minerals

Rapid immobilisation of chemical reactions in alkali-activated materials using solely microwave irradiation

Anže Tesovnik [1,2] and Barbara Horvat [3]

[1] Slovenian National Building and Civil Engineering Institute, Dimičeva ulica 12, Ljubljana, Slovenia; anze.tesovnik@zag.si
[2] Jožef Stefan International Postgraduate School, Jamova 39, 1000 Ljubljana, Slovenia
[3] Milan Vidmar Electric Power Research Institute, Hajdrihova 2, 1000 Ljubljana, Slovenia
* Correspondence: barbara.horvat@eimv.si

The minerals present in the precursors are shown in Table S1.

Table S1. XRD reference mineral cards and corresponding chemical formulas used for the analysis of XRD patterns of precursors with the amount of amorphous content.

Precursor	Mineral name	Mineral [m%]	Reference code	Chemical formula	Amorphous content [m%]
SA	Calcite	19.4	ICSD 98-007-3446	$CaCO_3$	/
	Larnite	14.7	ICSD 98-042-1708	Ca_2SiO_4	/
	Sylvine, sodian	1.7	ICSD 98-024-0579	$ClK_{0.2}Na_{0.8}$	/
	Quartz	12.8	ICSD 98-008-3849	SiO_2	
	Brucite	1	ICSD 98-020-3212	H_2MgO_2	/
	/	/	/	/	49.6
GW	/	/	/	/	100.0
RW	Quartz	0.4	ICSD 98-008-3849	SiO_2	/
	/	/	/	/	99.6
FA	Quartz	7.3	ICSD 98-008-9277	SiO_2	/
	Magnetite	3.2	ICSD 98-015-8743	Fe_3O_4	/
	Hematite	1.9	ICSD 98-018-4766	Fe_2O_3	/
	Mullite	8.5	ICSD 98-015-8097	$Al_{2.41}Si_{0.59}O_{4.793}$	/
	Anhydrite	2.3	ICSD 98-001-6382	CaO_4S	/
	/	/	/	/	76.8
MK	Mullite	18.1	ICSD 98-015-8098	$Al_{2.34}Si_{0.66}O_{4.83}$	/
	Quartz	2.4	ICSD 98-015-6196	SiO_2	/

	Cristobalite	4.1	ICSD 98-016-2660	SiO_2	/
	/	/	/	/	74.5

The particle size distributions (PSDs) of the precursors measured using laser diffraction granulomeres are presented in Table S2.

Table S2. PSD summary for precursors SA, GW, RW, FA, and MK, including the mean diameter (MD), considering the volume of particles and main percentiles (d_{10}, d_{50}, and d_{90}).

	SA	GW	RW	FA	MK
MD [μm]	158.9	34.85	25.19	56.03	4.94
d_{10} [μm]	25.69	4.65	3.94	1.694	0.741
d_{50} [μm]	153.5	18.44	18.33	35.12	2.689
d_{90} [μm]	272	95.45	56.1	151	12.04

The irradiation time of the AAMs at 100 W and the mass loss owing to rapid dehydration are presented in Table S1. The dehydration time for mixtures with higher liquid content increased when compared to optimal mixtures, whereas that for mixtures with a lower amount of liquid phase than optimal was comparable to mixtures with an optimal amount of liquid (mixtures X.3 in Table 2).

Mass loss owing to irradiation was attributed to the rapid loss of water, which was still present in the AAM on day 7. The remaining water (the difference between the mass percentage of water in the slurry and the mass loss owing to irradiation) was lost during curing (Table S3).

Table S3. Total dehydration time and mass owing due to the irradiation of 7-day-old AAM mixtures at a constant microwave power of 100 W. Initial amount of water in the slurry and loss of water owing to curing.

Precursor label	Mixture label	Time of dehydration [min]	Mass loss [m%]	H_2O in slurry [g]	Slurry [g]	H_2O/slurry [m%]	H_2O lost during curing [m%]
SA	**1.1.**	15.0	5.9	27.8	150	18.5	12.6
SA	**1.2.**	26.0	15.9	55.6	200	27.8	11.9
SA	**1.3.**	15.5	5.2	19.5	135	14.4	9.2
GW	**2.1.**	16.0	9.8	27.8	150	18.5	8.7
GW	**2.2.**	29.0	15.4	55.6	200	27.8	12.4
GW	**2.3.**	18.0	13.1	44.5	180	24.7	11.6
RW	**3.1.**	24.0	9.6	27.8	150	18.5	9.0
RW	**3.2.**	30.0	15.1	55.6	200	27.8	12.8
RW	**3.3.**	24.0	11.3	44.5	180	24.7	13.4
FA	**4.1.**	18.0	9.3	27.8	150	18.5	9.2
FA	**4.2.**	26.0	16.6	55.6	200	27.8	11.2
FA	**4.3.**	22.0	7.8	19.5	135	14.4	6.6
MK	**5.1.**	-	-	-	-	-	-
MK	**5.2.**	30.0	15.8	55.6	200	27.8	12.0
MK	**5.3.**	33.0	17.7	66.7	220	30.3	12.6

The stored fragments exposed to ambient conditions after 30 days are presented in Figure S1. Salt in crystalline form became visible to the naked eye after 30 days for the non-dehydrated prism fragments of SA, RW, and GW with a chemical composition that could lead to efflorescence in the presence of water/moisture (Table 3: mixtures FA 4.3. and MK 5.2. are the only mixtures that have the theoretical potential to not lead to efflorescence when alkali elements from 1st and 2nd group of PS are considered). White spots appeared on the surface of the microwave-dehydrated samples immediately after

irradiation (Figure 4), indicating that the alkali elements were still mobile (not bonded in the aluminosilicate network). However, for the dehydrated samples, no additional naked-eye-visible surface salt was formed after 30 days. The lack of further development of efflorescence indicates that dehydration successfully hindered further evolution of the material, but only over a short period under ambient conditions (in the presence of ambient moisture).

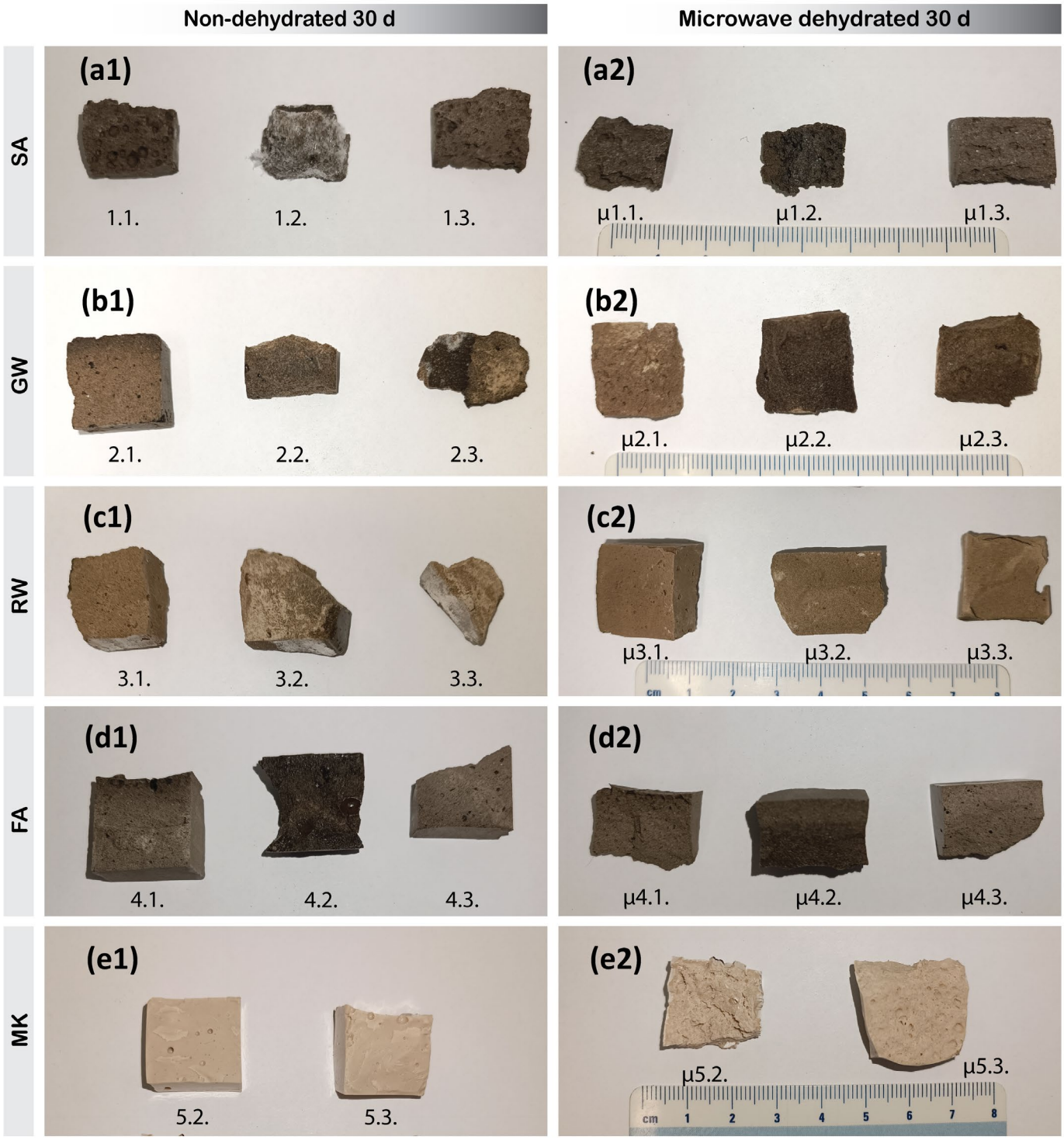

Figure S1. Fragments of prisms after mechanical property testing on day 7, exposed to ambient conditions for 30 days.

The 7-day-old geometrical density, along with the bulk and skeletal densities, is presented in Figure S2. The geometrical density decreased after dehydration, with a decrease in the mass of the sample (water was removed; Table S3, Figure S3), regardless of volume changes. New cracks and pores were formed inside the prism owing to the increased pressure caused by the transformation of water from the liquid to the gaseous state; however, several samples exhibited overall shrinkage (Figure S3). Because prisms of irradiated samples can twist, curve, or 'slightly' reshape, but not evenly throughout the volume (owing to the electromagnetic field in the microwave chamber having unevenly distributed nods), the volume (length, height, width of the prism) can have significant error. Therefore, the geometrical density of the irradiated samples had a larger error, and only their true geometrical density could be larger.

In contrast to the geometrical density, the skeletal and bulk densities (both measured by MIP) highly depend on the choice of the fraction of the sample and not on its shape. Therefore, the measurement of the bulk density of the irradiated samples is more accurate than that of the geometrical density; however, MIP cannot detect large pores and cracks that form during irradiation. Therefore, the true density of the overall sample was between the geometric and bulk densities. The larger the difference between the geometrical and bulk densities, the more severely the sample is damaged by irradiation.

From Figure S2b, it can be concluded that the higher skeletal and bulk/geometrical densities of the non-irradiated samples are not necessarily related to the higher compressive strength, but to the precursor used. Both wools (RW and GW) have the highest amount of amorphous content (approximately 100%, Figure 2), are milled below 63 μm, and reach the highest compressive strengths. FA and MK have 'only' 75% amorphous content and are used as received, where non-irradiated AAM from MK has a higher bulk density (less porous material, see Figure S4), and AAM from FA has a higher skeletal density, which results in AAM from FA exhibiting a higher compressive strength than AAM from MK (Figure S2b). In contrast, SA had less than 50% amorphous content and was not as fine as RW, GW, FA, or MK (PSD in Figure 3). High densities of alkali-activated SA originate from the precursor SA itself but do not contribute to the aluminosilicate network or compressive strength. The high amount of minerals in SA is only suitable as a filler for AAM.

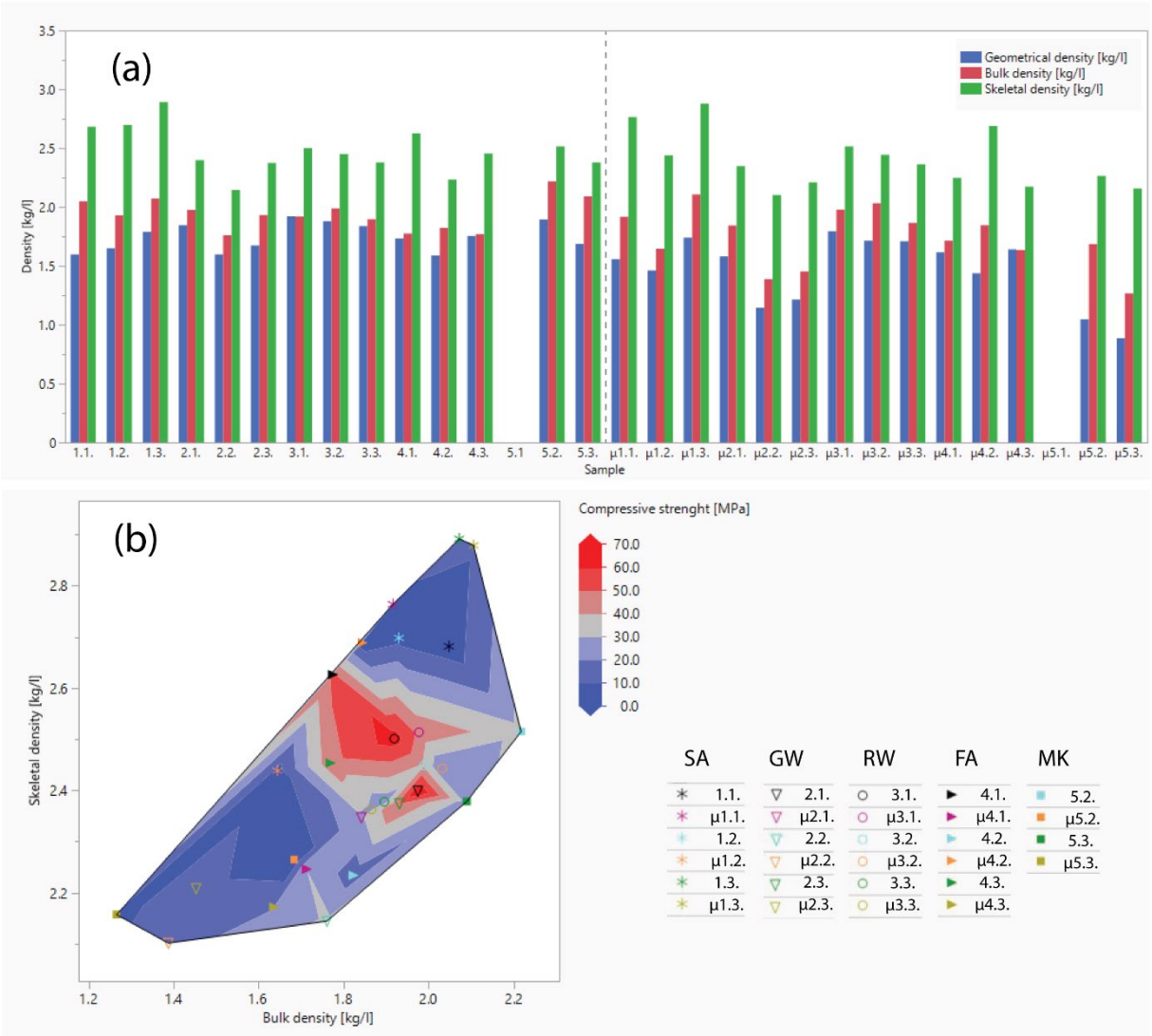

Figure S2. Geometric, bulk, and skeletal densities of all prepared AAMs (a). Contour plot illustrating the relationship between bulk and skeletal density and their influence on compressive strength (b). Colour gradient (Delaunay triangulation) represents compressive strength, with red and blue indicating higher and lower strengths, respectively.

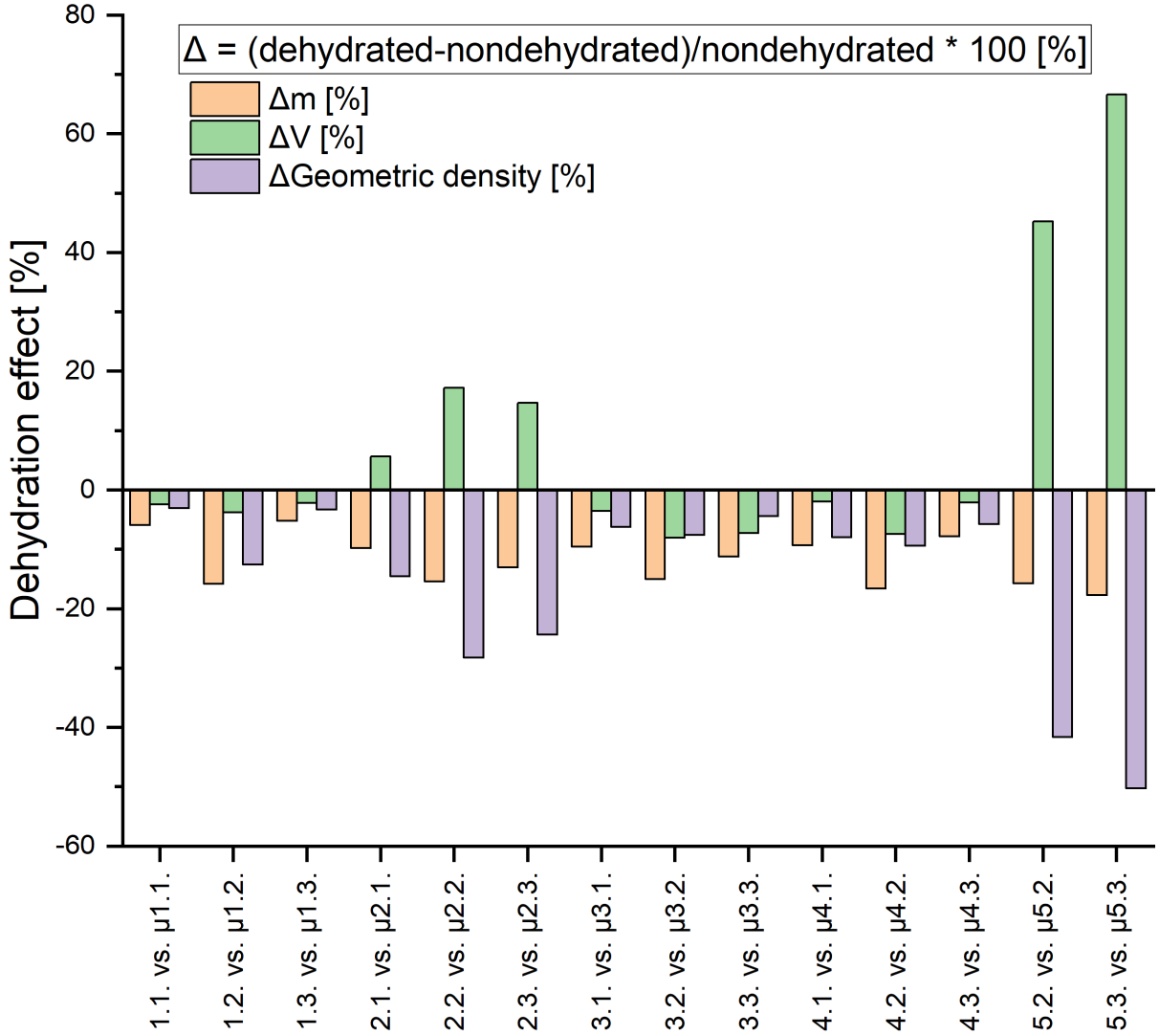

Figure S3. Effect of dehydration on mass, volume, and geometrical density.

The MIP results are presented in Figure S4. Significant changes in pore distribution and total porosity owing to irradiation were observed in all samples except in samples from RW, which was also confirmed by the naked eye and SEM observations (Figures 4 and 6, respectively). However, MIP cannot detect pores larger than 380 µm (and smaller than 1 nm), which were present in irradiated samples (as in case µ5.2. in Figure 4). In addition, the electromagnetic field in the microwave does not affect the material evenly throughout the microwave chamber (regardless of the presence of the turntable), because hot spots are present only at a few permanent locations (the electromagnetic wave is standing). Therefore, in the case of irradiated samples, the total porosity may exceed the measured values and the pore distribution can have additional peaks above 380 µm.

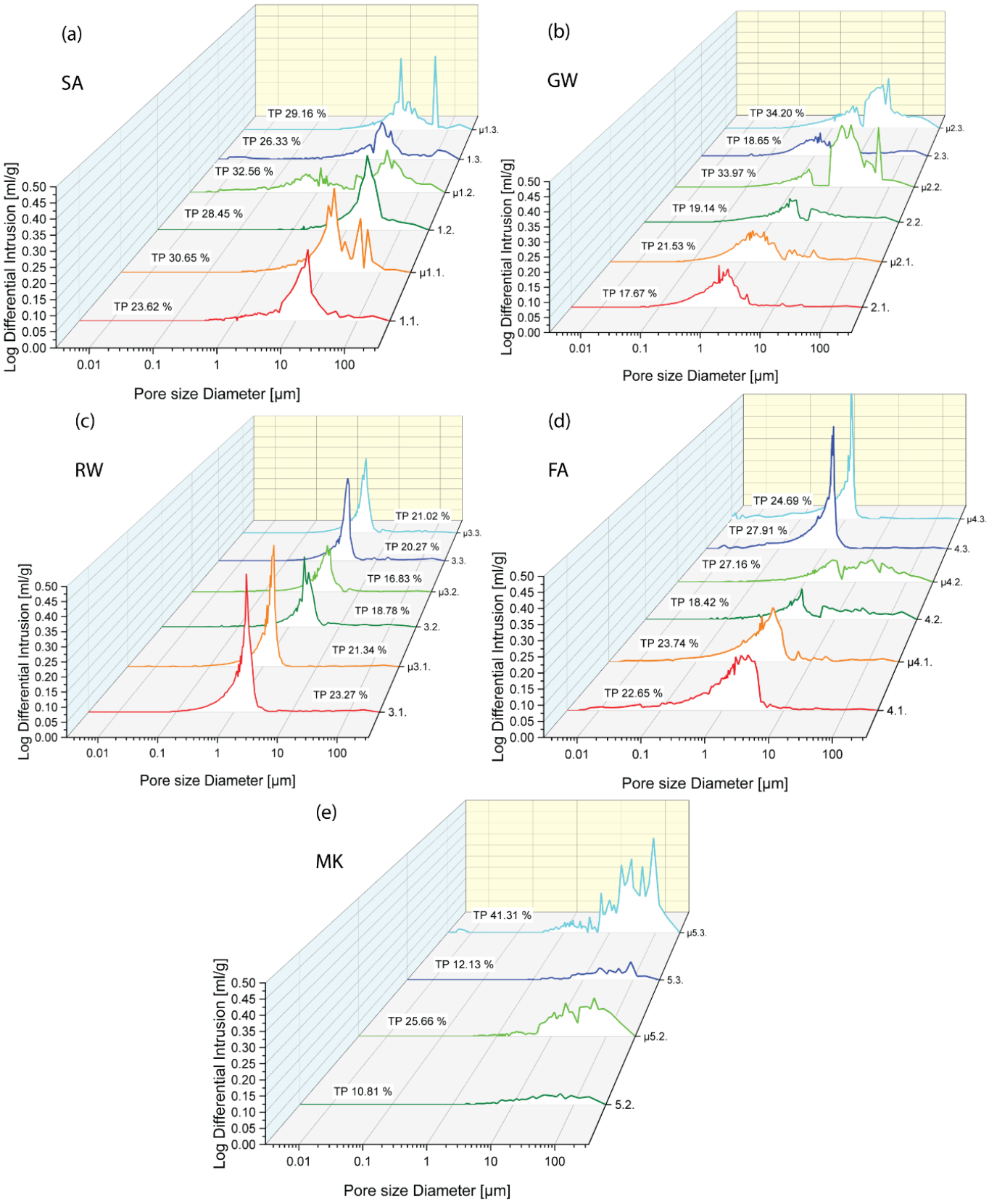

Figure S4. Pore size distribution of AAMs made of a) SA, b) GW, c) RW, d) FA, and e) MK. Total porosity (TP) is given as the proportion of pores to the volume of material. Samples dehydrated with microwaves are marked with μ.

The XRD patterns of the 14-day-old and 1-year-old AAMs are shown in Figure S5. For all mixtures of different precursors, it was observed that no new crystalline phases were formed upon microwave dehydration of the samples after 14 days, and that any potentially formed salt was above the XRD detection limit.

In the case of 1-year-old samples, peaks of newly formed crystalline efflorescence were observed in the range of 30–45° (Figure S5a2, b2, c2, d2, e2). The peaks corresponding to the crystalline sodium carbonate mineral thermonatrite [115], [116] were most pronounced in the mixtures with the highest amount of alkali.

For the slag mixtures, FTIR detected early signs of efflorescence development after 14 days in the non-dehydrated samples (Figure 7a1). However, XRD did not detect any clear crystalline salt formation at 14 days, which can be attributed to the (i) XRD detection limit, (ii) overlapping of peaks, or (iii) amorphous clusters of future crystalline salts not yet being crystallised (Figure S5a2).

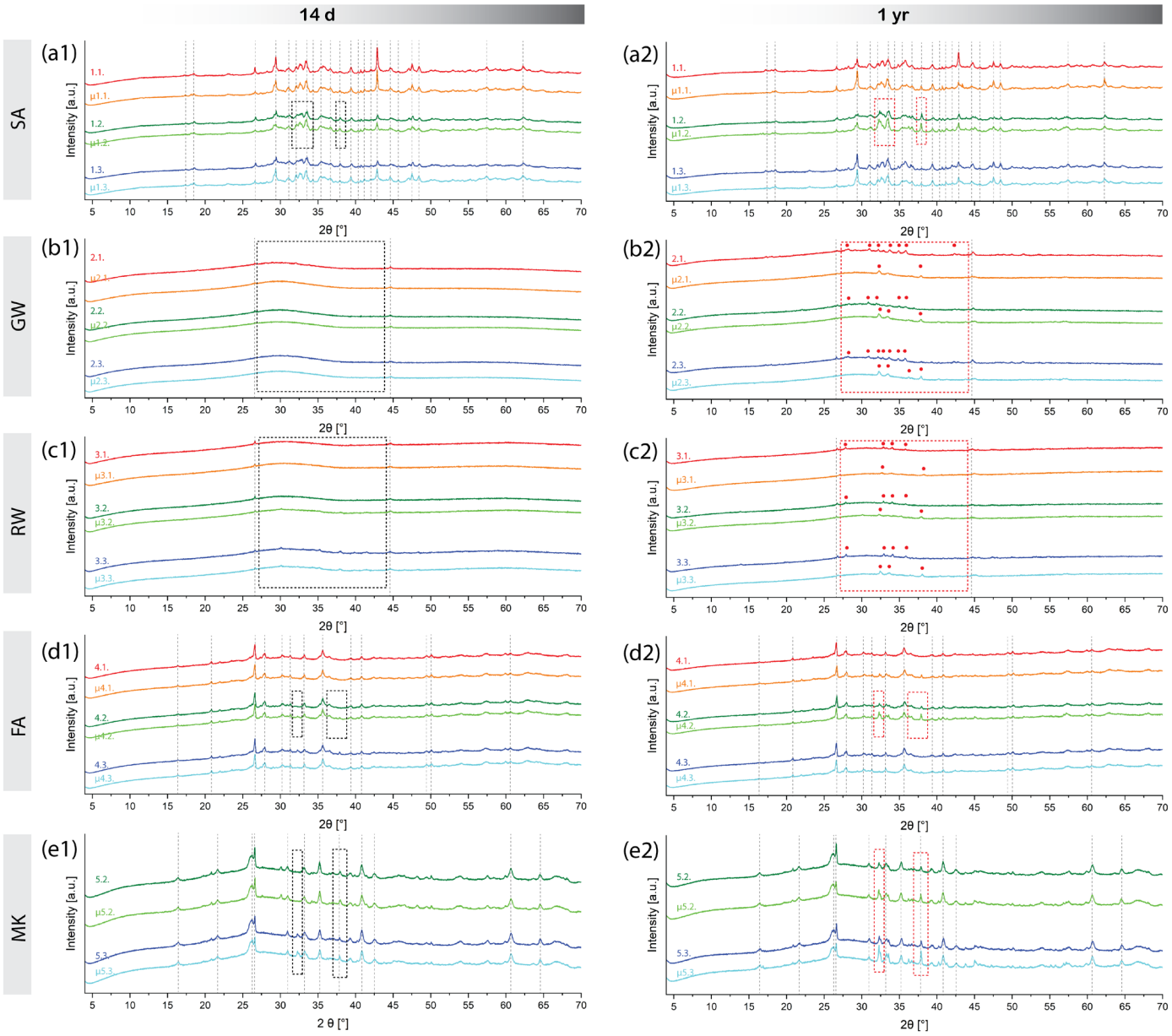

Figure S5. The XRD patterns of 14-day-old (left) and 1-year-old (right) AAMs made of a) SA, b) GW, c) RW, d) FA, and e) MK. Samples dehydrated with microwaves are marked with μ.

As shown in Figure S6, when a drop is added to 1-year-old microwave-dehydrated samples, Na is visibly precipitated, while the other measured elements K, Ca, and Mg are not precipitated on the surface.

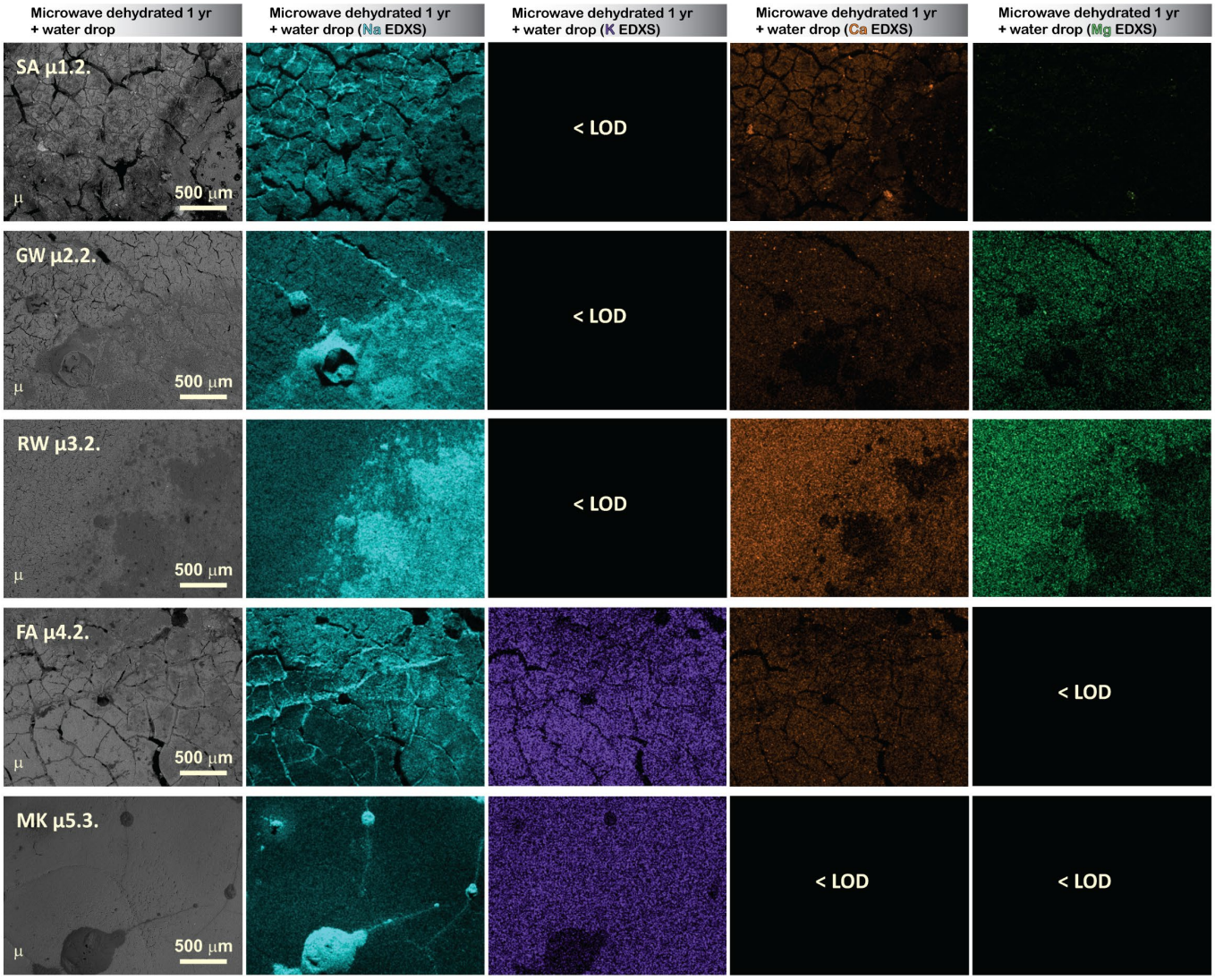

Figure S6. SEM-EDXS mapping on 1-year-old dehydrated samples for the elements sodium (Na), potassium (K), calcium (Ca), and magnesium (Mg).

Micrographs of the dried edge remaining on the surface of 1-month-old sample 2.2 after drying of the water droplet and IPA are shown in Figure S7. In the case of the distilled water droplet, salt formations up to 100 µm in size formed at the edge of the contact between the droplet and the sample after 90 min (Figure S7a), which was also confirmed by EDXS spot analysis, showing higher Na concentrations in the edge region (indicated by the circle) than in the region not in contact with water (indicated by the x). In the case of the IPA droplet, the edge is observed as a dark line where an efflorescence of up to 20 µm is visible (Fig. S7b). In addition to the increased amount of Na, more carbon is also observed, which may indicate the removal of volatile organic compounds [117] from the sample made of the GW precursor, which has the most organic matter according to the LOI data (Table 1).

The drying of a drop of distilled water on the surface of the sample can be seen in full at the end of the Supplementary Material in Video 2 (due to the length of time, the video is sped up 10 x), and the IPA droplet in Video 3.

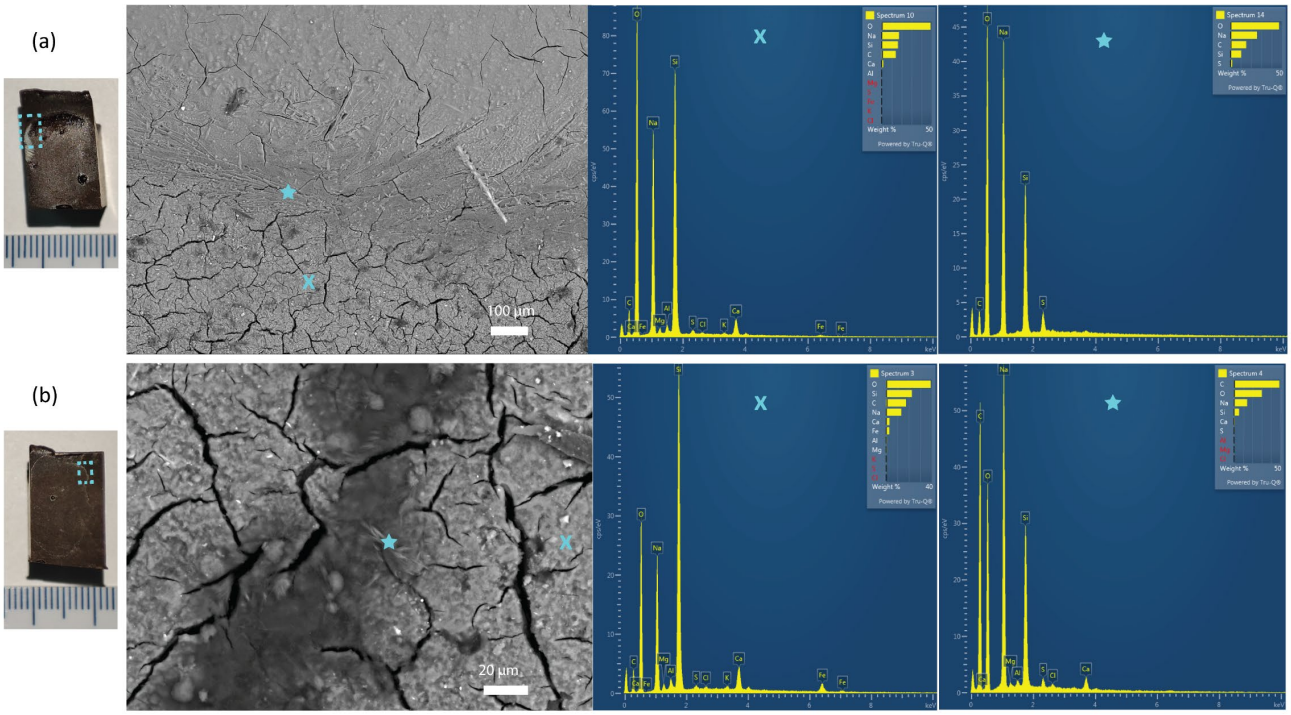

Figure S7. SEM image of the remaining traces after droplet drying: (a) distilled water and (b) IPA, and EDXS spot analysis.

As can be seen in Table S3, the pH and EC of the immersion medium increased with time, indicating leaching of free alkali from sample 2.2. In the IPA medium, the process is only detected to a lesser extent. The start and progress of immersion in IPA and distilled water are recorded in Video 3 at the end of the Supplementary Material.

Table S4. Detailed data of electrical resistivity and temperature of EC and pH probes measuring immersion solution of sample 2.2. Owing to difficulties in pH measurements of hydroalcoholic solutions, the pH values of IPA immersion solution are only arbitrary numbers and marked with *.

Immersion media	Probe	Only immersion media	10 min	24 h	14 d
H_2O	pH	6.37 pH, T=23.4°C, 39.7 mV	11.33 pH, T=24.5°C, 247.5 mV	11.97 pH, T=24.4°C, -283.9 mV	12.05 pH, T=25.1°C, -289.6 mV
	EC	3.7 µS/cm, T=24.2°C, 146.8 KΩ	2727.0 µS/cm, T=23.7°C, 198.6 Ω	14637.7 µS/cm,T=25.9°C, 35.4 Ω	23043.8 µS/cm,T=25.2°C, 22.8 Ω
IPA	pH	6.58 pH*, T=23.2°C, 27.4 mV	9.21 pH*, T=25.9°C, -128.4 mV	10.41 pH*, T=25.8°C, -194.9 mV	10.68 pH*, T=25.0°C, -234.9 mV
	EC	0 µS/cm, T=24.2°C, 28.67 MΩ	0.3 µS/cm, T=24.4°C, 1766.0 kΩ	1.6 µS/cm, T=25.3°C, 334.0 kΩ	3.6 µS/cm, T=25.2°C, 114.7 kΩ

References

115. L. Simão, D. Hotza, F. Raupp-Pereira, M. Ribeiro, O. Montedo, and É. Fernandes, "Controlling efflorescence in geopolymers: A new approach," *Case Studies in Construction Materials*, vol. 15, Oct. 2021, doi: 10.1016/j.cscm.2021.e00740.
116. J. Fořt, M. Mildner, M. Keppert, and R. Černý, "Waste solidified alkalis as activators of aluminosilicate precursors: Functional and environmental evaluation," *Journal of Building Engineering*, vol. 54, p. 104598, Aug. 2022, doi: 10.1016/j.jobe.2022.104598.

117. R. Abbas-Ghaleb and D. Chlala, "Catalytic oxidation of isopropyl alcohol over platinum based catalyst: A study of the effect of methyl cellulose on Pt particles dispersion over mullite," *Braz. J. Chem. Eng.*, vol. 36, no. 3, pp. 1175–1184, Jul. 2019, doi: 10.1590/0104-6632.20190363s20190023.